

Circumferential optical coherence tomography angiography imaging of the swine esophagus using a micromotor balloon catheter

HSIANG-CHIEH LEE,¹ OSMAN OGUZ AHSEN,¹ KAICHENG LIANG,¹ ZHAO WANG,¹ CODY CLEVELAND,^{2,3,4} LUCAS BOOTH,^{2,3} BENJAMIN POTSAID,^{1,5} VIJAYSEKHAR JAYARAMAN,⁶ ALEX E. CABLE,⁵ HIROSHI MASHIMO,^{7,8} ROBERT LANGER,^{2,3} GIOVANNI TRAVERSO,^{2,3,4,7} AND JAMES G. FUJIMOTO^{1,*}

¹Department of Electrical Engineering & Computer Science and Research Laboratory of Electronics, Massachusetts Institute of Technology, Cambridge MA, USA

²Koch Institute for Integrative Cancer Research, Massachusetts Institute of Technology, Cambridge MA, USA

³Department of Chemical Engineering, Massachusetts Institute of Technology, Cambridge MA, USA

⁴Brigham and Women's Hospital, Boston MA, USA

⁵Advanced Imaging Group, Thorlabs Inc., Newton NJ, USA

⁶Praevium Research Inc., Santa Barbara CA, USA

⁷Harvard Medical School, Boston, MA, USA

⁸Veterans Affairs Boston Healthcare System, Boston MA, USA

*jgfiji@mit.edu

Abstract: We demonstrate a micromotor balloon imaging catheter for ultrahigh speed endoscopic optical coherence tomography (OCT) which provides wide area, circumferential structural and angiographic imaging of the esophagus without contrast agents. Using a 1310 nm MEMS tunable wavelength swept VCSEL light source, the system has a 1.2 MHz A-scan rate and $\sim 8.5 \mu\text{m}$ axial resolution in tissue. The micromotor balloon catheter enables circumferential imaging of the esophagus at 240 frames per second (fps) with a $\sim 30 \mu\text{m}$ (FWHM) spot size. Volumetric imaging is achieved by proximal pullback of the micromotor assembly within the balloon at 1.5 mm/sec. Volumetric data consisting of 4200 circumferential images of 5,000 A-scans each over a 2.6 cm length, covering a $\sim 13 \text{ cm}^2$ area is acquired in <18 seconds. A non-rigid image registration algorithm is used to suppress motion artifacts from non-uniform rotational distortion (NURD), cardiac motion or respiration. *En face* OCT images at various depths can be generated. OCT angiography (OCTA) is computed using intensity decorrelation between sequential pairs of circumferential scans and enables three-dimensional visualization of vasculature. Wide area volumetric OCT and OCTA imaging of the swine esophagus *in vivo* is demonstrated.

©2016 Optical Society of America

OCIS codes: (110.6880) Three-dimensional image acquisition; (170.2150) Endoscopic imaging; (170.2680) Gastrointestinal; (170.3880) Medical and biological imaging; (170.4500) Optical coherence tomography.

References and links

1. D. Huang, E. A. Swanson, C. P. Lin, J. S. Schuman, W. G. Stinson, W. Chang, M. R. Hee, T. Flotte, K. Gregory, C. A. Puliafito, and J. G. Fujimoto, "Optical coherence tomography," *Science* **254**(5035), 1178–1181 (1991).
2. B. E. Bouma, G. J. Tearney, C. C. Compton, and N. S. Nishioka, "High-resolution imaging of the human esophagus and stomach *in vivo* using optical coherence tomography," *Gastrointest. Endosc.* **51**(4), 467–474 (2000).
3. M. V. Sivak, Jr., K. Kobayashi, J. A. Izatt, A. M. Rollins, R. Ung-Runyawee, A. Chak, R. C. Wong, G. A. Isenberg, and J. Willis, "High-resolution endoscopic imaging of the GI tract using optical coherence tomography," *Gastrointest. Endosc.* **51**(4), 474–479 (2000).
4. X. D. Li, S. A. Boppart, J. Van Dam, H. Mashimo, M. Mutinga, W. Drexler, M. Klein, C. Pitris, M. L. Krinsky, M. E. Brezinski, and J. G. Fujimoto, "Optical coherence tomography: advanced technology for the endoscopic imaging of Barrett's esophagus," *Endoscopy* **32**(12), 921–930 (2000).

5. B. J. Vakoc, M. Shishko, S. H. Yun, W.-Y. Oh, M. J. Suter, A. E. Desjardins, J. A. Evans, N. S. Nishioka, G. J. Tearney, and B. E. Bouma, "Comprehensive esophageal microscopy by using optical frequency-domain imaging (with video)," *Gastrointest. Endosc.* **65**(6), 898–905 (2007).
6. M. J. Suter, B. J. Vakoc, P. S. Yachimski, M. Shishkov, G. Y. Lauwers, M. Mino-Kenudson, B. E. Bouma, N. S. Nishioka, and G. J. Tearney, "Comprehensive microscopy of the esophagus in human patients with optical frequency domain imaging," *Gastrointest. Endosc.* **68**(4), 745–753 (2008).
7. H. L. Fu, Y. Leng, M. J. Cobb, K. Hsu, J. H. Hwang, and X. Li, "Flexible miniature compound lens design for high-resolution optical coherence tomography balloon imaging catheter," *J. Biomed. Opt.* **13**(6), 060502 (2008).
8. J. Xi, L. Huo, Y. Wu, M. J. Cobb, J. H. Hwang, and X. Li, "High-resolution OCT balloon imaging catheter with astigmatism correction," *Opt. Lett.* **34**(13), 1943–1945 (2009).
9. W. Kang, H. Wang, Y. Pan, M. W. Jenkins, G. A. Isenberg, A. Chak, M. Atkinson, D. Agrawal, Z. Hu, and A. M. Rollins, "Endoscopically guided spectral-domain OCT with double-balloon catheters," *Opt. Express* **18**(16), 17364–17372 (2010).
10. S. H. Yun, G. J. Tearney, B. J. Vakoc, M. Shishkov, W. Y. Oh, A. E. Desjardins, M. J. Suter, R. C. Chan, J. A. Evans, I. K. Jang, N. S. Nishioka, J. F. de Boer, and B. E. Bouma, "Comprehensive volumetric optical microscopy *in vivo*," *Nat. Med.* **12**(12), 1429–1433 (2007).
11. D. C. Adler, Y. Chen, R. Huber, J. Schmitt, J. Connolly, and J. G. Fujimoto, "Three-dimensional endomicroscopy using optical coherence tomography," *Nat. Photonics* **1**(12), 709–716 (2007).
12. S. H. Yun, C. Boudoux, G. J. Tearney, and B. E. Bouma, "High-speed wavelength-swept semiconductor laser with a polygon-scanner-based wavelength filter," *Opt. Lett.* **28**(20), 1981–1983 (2003).
13. R. Huber, M. Wojtkowski, and J. G. Fujimoto, "Fourier Domain Mode Locking (FDML): A new laser operating regime and applications for optical coherence tomography," *Opt. Express* **14**(8), 3225–3237 (2006).
14. T. Endo, T. Awakawa, H. Takahashi, Y. Arimura, F. Itoh, K. Yamashita, S. Sasaki, H. Yamamoto, X. Tang, and K. Imai, "Classification of Barrett's epithelium by magnifying endoscopy," *Gastrointest. Endosc.* **55**(6), 641–647 (2002).
15. D. C. Adler, C. Zhou, T. H. Tsai, H. C. Lee, L. Becker, J. M. Schmitt, Q. Huang, J. G. Fujimoto, and H. Mashimo, "Three-dimensional optical coherence tomography of Barrett's esophagus and buried glands beneath neosquamous epithelium following radiofrequency ablation," *Endoscopy* **41**(9), 773–776 (2009).
16. P. H. Tran, D. S. Mukai, M. Brenner, and Z. Chen, "In vivo endoscopic optical coherence tomography by use of a rotational microelectromechanical system probe," *Opt. Lett.* **29**(11), 1236–1238 (2004).
17. P. Herz, Y. Chen, A. Aguirre, J. Fujimoto, H. Mashimo, J. Schmitt, A. Koski, J. Goodnow, and C. Petersen, "Ultrahigh resolution optical biopsy with endoscopic optical coherence tomography," *Opt. Express* **12**(15), 3532–3542 (2004).
18. J. Su, J. Zhang, L. Yu, H. G. Colt, M. Brenner, and Z. Chen, "Real-time swept source optical coherence tomography imaging of the human airway using a microelectromechanical system endoscope and digital signal processor," *J. Biomed. Opt.* **13**(3), 030506 (2008).
19. J. Li, M. de Groot, F. Helderman, J. Mo, J. M. A. Daniels, K. Grünberg, T. G. Sutedja, and J. F. de Boer, "High speed miniature motorized endoscopic probe for optical frequency domain imaging," *Opt. Express* **20**(22), 24132–24138 (2012).
20. T.-H. Tsai, B. Potsaid, Y. K. Tao, V. Jayaraman, J. Jiang, P. J. S. Heim, M. F. Kraus, C. Zhou, J. Hornegger, H. Mashimo, A. E. Cable, and J. G. Fujimoto, "Ultrahigh speed endoscopic optical coherence tomography using micromotor imaging catheter and VCSEL technology," *Biomed. Opt. Express* **4**(7), 1119–1132 (2013).
21. T.-H. Tsai, O. O. Ahsen, H.-C. Lee, K. Liang, M. Figueiredo, Y. K. Tao, M. G. Giacomelli, B. M. Potsaid, V. Jayaraman, Q. Huang, A. E. Cable, J. G. Fujimoto, and H. Mashimo, "Endoscopic Optical Coherence Angiography Enables 3-Dimensional Visualization of Subsurface Microvasculature," *Gastroenterology* **147**(6), 1219–1221 (2014).
22. V. Jayaraman, J. Jiang, H. Li, P. J. S. Heim, G. D. Cole, B. Potsaid, J. G. Fujimoto, and A. Cable, "OCT imaging up to 760 kHz axial scan rate using single-mode 1310nm MEMS-tunable VCSELs with >100nm tuning range," in *Lasers and Electro-Optics (CLEO), 2011 Conference on*, 2011, 1–2.
23. T. Wang, W. Wieser, G. Springeling, R. Beurskens, C. T. Lancee, T. Pfeiffer, A. F. W. van der Steen, R. Huber, and G. van Soest, "Intravascular optical coherence tomography imaging at 3200 frames per second," *Opt. Lett.* **38**(10), 1715–1717 (2013).
24. O. O. Ahsen, H.-C. Lee, M. G. Giacomelli, Z. Wang, K. Liang, T.-H. Tsai, B. Potsaid, H. Mashimo, and J. G. Fujimoto, "Correction of rotational distortion for catheter-based en face OCT and OCT angiography," *Opt. Lett.* **39**(20), 5973–5976 (2014).
25. S. Makita, Y. Hong, M. Yamanari, T. Yatagai, and Y. Yasuno, "Optical coherence angiography," *Opt. Express* **14**(17), 7821–7840 (2006).
26. R. K. Wang, S. L. Jacques, Z. Ma, S. Hurst, S. R. Hanson, and A. Gruber, "Three dimensional optical angiography," *Opt. Express* **15**(7), 4083–4097 (2007).
27. R. Reif and R. K. Wang, "Optical Microangiography Based on Optical Coherence Tomography," in *Optical Coherence Tomography: Technology and Applications*, W. Drexler and G. J. Fujimoto, eds. (Springer International Publishing, Cham, 2015), pp. 1373–1397.
28. Y. Wang and R. Wang, "Autocorrelation optical coherence tomography for mapping transverse particle-flow velocity," *Opt. Lett.* **35**(21), 3538–3540 (2010).
29. E. Jonathan, J. Enfield, and M. J. Leahy, "Correlation mapping method for generating microcirculation morphology from optical coherence tomography (OCT) intensity images," *J. Biophotonics* **4**(9), 583–587 (2011).

30. Y. Jia, O. Tan, J. Tokayer, B. Potsaid, Y. Wang, J. J. Liu, M. F. Kraus, H. Subhash, J. G. Fujimoto, J. Hornegger, and D. Huang, "Split-spectrum amplitude-decorrelation angiography with optical coherence tomography," *Opt. Express* **20**(4), 4710–4725 (2012).
31. A. Mariampillai, B. A. Standish, E. H. Moriyama, M. Khurana, N. R. Munce, M. K. K. Leung, J. Jiang, A. Cable, B. C. Wilson, I. A. Vitkin, and V. X. D. Yang, "Speckle variance detection of microvasculature using swept-source optical coherence tomography," *Opt. Lett.* **33**(13), 1530–1532 (2008).
32. J. Enfield, E. Jonathan, and M. Leahy, "In vivo imaging of the microcirculation of the volar forearm using correlation mapping optical coherence tomography (cmOCT)," *Biomed. Opt. Express* **2**(5), 1184–1193 (2011).
33. V. X. D. Yang, S. J. Tang, M. L. Gordon, B. Qi, G. Gardiner, M. Cirocco, P. Kortan, G. B. Haber, G. Kandel, I. A. Vitkin, B. C. Wilson, and N. E. Marcon, "Endoscopic Doppler optical coherence tomography in the human GI tract: initial experience," *Gastrointest. Endosc.* **61**(7), 879–890 (2005).
34. K. Liang, G. Traverso, H. C. Lee, O. O. Ahsen, Z. Wang, B. Potsaid, M. Giacomelli, V. Jayaraman, R. Barman, A. Cable, H. Mashimo, R. Langer, and J. G. Fujimoto, "Ultrahigh speed en face OCT capsule for endoscopic imaging," *Biomed. Opt. Express* **6**(4), 1146–1163 (2015).
35. J. Mavadia, J. Xi, Y. Chen, and X. Li, "An all-fiber-optic endoscopy platform for simultaneous OCT and fluorescence imaging," *Biomed. Opt. Express* **3**(11), 2851–2859 (2012).
36. W. Kang, H. Wang, Z. Wang, M. W. Jenkins, G. A. Isenberg, A. Chak, and A. M. Rollins, "Motion artifacts associated with in vivo endoscopic OCT images of the esophagus," *Opt. Express* **19**(21), 20722–20735 (2011).
37. N. Uribe-Patarroyo and B. E. Bouma, "Rotational distortion correction in endoscopic optical coherence tomography based on speckle decorrelation," *Opt. Lett.* **40**(23), 5518–5521 (2015).
38. M. Guizar-Sicairos, S. T. Thurman, and J. R. Fienup, "Efficient subpixel image registration algorithms," *Opt. Lett.* **33**(2), 156–158 (2008).
39. M. F. Kraus, B. Potsaid, M. A. Mayer, R. Bock, B. Baumann, J. J. Liu, J. Hornegger, and J. G. Fujimoto, "Motion correction in optical coherence tomography volumes on a per A-scan basis using orthogonal scan patterns," *Biomed. Opt. Express* **3**(6), 1182–1199 (2012).
40. Z. Wang, M. Jenkins, G. Linderman, H. Bezerra, Y. Fujino, M. Costa, D. Wilson, and A. Rollins, "3-D Stent Detection in Intravascular OCT Using a Bayesian Network and Graph Search," *IEEE Trans. Med. Imaging* **34**(7), 1549–1561 (2015).
41. M. A. Kara, M. Ennahachi, P. Fockens, F. J. W. ten Kate, and J. J. G. H. M. Bergman, "Detection and classification of the mucosal and vascular patterns (mucosal morphology) in Barrett's esophagus by using narrow band imaging," *Gastrointest. Endosc.* **64**(2), 155–166 (2006).
42. R. Kiesslich, L. Gossner, M. Goetz, A. Dahlmann, M. Vieth, M. Stolte, A. Hoffman, M. Jung, B. Nafe, P. R. Galle, and M. F. Neurath, "In vivo histology of Barrett's esophagus and associated neoplasia by confocal laser endomicroscopy," *Clin. Gastroenterol. Hepatol.* **4**(8), 979–987 (2006).
43. P. Sharma, R. H. Hawes, A. Bansal, N. Gupta, W. Curvers, A. Rastogi, M. Singh, M. Hall, S. C. Mathur, S. B. Wani, B. Hoffman, S. Gaddam, P. Fockens, and J. J. Bergman, "Standard endoscopy with random biopsies versus narrow band imaging targeted biopsies in Barrett's oesophagus: a prospective, international, randomised controlled trial," *Gut* **62**(1), 15–21 (2013).
44. M. J. Gora, J. S. Sauk, R. W. Carruth, W. Lu, D. T. Carlton, A. Soomro, M. Rosenberg, N. S. Nishioka, and G. J. Tearney, "Imaging the upper gastrointestinal tract in unsedated patients using tethered capsule endomicroscopy," *Gastroenterology* **145**(4), 723–725 (2013).
45. A. Couvelard, F. Paraf, V. Gratio, J.-Y. Scoazec, D. Hénin, C. Degott, and J. F. Fléjou, "Angiogenesis in the neoplastic sequence of Barrett's oesophagus. Correlation with VEGF expression," *J. Pathol.* **192**(1), 14–18 (2000).
46. V. Becker, M. Vieth, M. Bajbouj, R. M. Schmid, and A. Meining, "Confocal laser scanning fluorescence microscopy for in vivo determination of microvessel density in Barrett's esophagus," *Endoscopy* **40**(11), 888–891 (2008).
47. S. Yun, G. Tearney, J. de Boer, and B. Bouma, "Removing the depth-degeneracy in optical frequency domain imaging with frequency shifting," *Opt. Express* **12**(20), 4822–4828 (2004).
48. Z. Wang, H. C. Lee, D. Vermeulen, L. Chen, T. Nielsen, S. Y. Park, A. Ghaemi, E. Swanson, C. Doerr, and J. Fujimoto, "Silicon photonic integrated circuit swept-source optical coherence tomography receiver with dual polarization, dual balanced, in-phase and quadrature detection," *Biomed. Opt. Express* **6**(7), 2562–2574 (2015).
49. M. J. Suter, P. A. Jillella, B. J. Vakoc, E. F. Halpern, M. Mino-Kenudson, G. Y. Lauwers, B. E. Bouma, N. S. Nishioka, and G. J. Tearney, "Image-guided biopsy in the esophagus through comprehensive optical frequency domain imaging and laser marking: a study in living swine," *Gastrointest. Endosc.* **71**(2), 346–353 (2010).
50. K. Beaudette, H. W. Baac, W. J. Madore, M. Villiger, N. Godbout, B. E. Bouma, and C. Boudoux, "Laser tissue coagulation and concurrent optical coherence tomography through a double-clad fiber coupler," *Biomed. Opt. Express* **6**(4), 1293–1303 (2015).

1. Introduction

Optical coherence tomography (OCT) can provide real time, depth resolved imaging of tissue with micron scale resolution [1]. Using fiber optic scanning catheters, *in vivo* endoscopic OCT imaging of the human gastrointestinal (GI) tract was demonstrated by several groups over a decade ago [2–4]. Although the fiber optic catheters in these studies were small enough to pass through the accessory port of an endoscope, imaging coverage was very limited. To

increase the coverage, an OCT balloon imaging catheter was first proposed in 2000 [4] and subsequently demonstrated in living swine and human esophagus [5, 6]. In contrast to positioning a small diameter imaging catheter over quadrants of the esophageal surface, the balloon catheter allows full circumferential imaging by centering the optics and expanding the esophageal lumen. Circumferential beam scanning was originally implemented with proximal rotary actuation transmitted by a torque cable housing the optical fiber. Later studies demonstrated an optical design using miniature compound gradient-index rod lenses to achieve a small focused spot size ($\sim 39 \mu\text{m}$, full width at half maximum (FWHM)) at a ~ 9 mm working distance [7]. In addition, high resolution balloon OCT imaging was achieved by correcting the astigmatism from the plastic sheath with a cylindrical aluminum reflector [8]. An alternative double balloon sheath design was proposed to allow endoscopic OCT imaging of the esophageal mucosa either with or without direct balloon contact to the tissue [9].

The increased imaging coverage of balloon catheters requires sufficient speed for Nyquist A-scan sampling along the balloon circumference, without sacrificing the circumferential beam scanning speed. The development of Fourier domain detection techniques and high speed, wavelength swept light sources has greatly improved the imaging speed and detection sensitivity of OCT systems, enabling volumetric endoscopic OCT imaging [10, 11]. Using a high speed, wavelength swept light source based on a polygon mirror filter [12], early studies demonstrated volumetric endoscopic OCT of the esophagus and coronary arteries in living swine at an A-scan rate of 64 kHz [10]. In parallel, studies also demonstrated volumetric imaging in the rabbit GI tract using a high speed endoscopic OCT system with a Fourier domain mode-locked (FDML) laser at an A-scan rate of 100 kHz [11]. The FDML laser uses a synchronously tuned fiber-based Fabry-Perot tunable filter (FFP-TF) and a long fiber delay line inside a ring fiber cavity, enabling high speed wavelength sweeps with narrow linewidth and high output power [13]. However, visualization of clinically relevant features in these volumetric endoscopic OCT systems was largely limited to cross-sectional OCT frames because of the limited catheter scanning speeds and OCT system imaging speeds.

Volumetric *en face* OCT imaging enables rapid examination of mucosal surface patterns similar to conventional white light endoscopy (WLE) which are known markers of GI neoplasms [14] but with the ability to visualize sub-surface features [11, 15]. However, limited imaging speed and instabilities in conventional proximal actuation scanning make images vulnerable to motion artifacts and nonuniform rotational distortion (NURD). Therefore, volumetric *en face* OCT is challenging with endoscopic OCT systems that use a proximally actuated catheter, especially in balloon catheters which have long working distances that increase the effects of scanning instability. NURD in OCT images can be significantly reduced using catheters with distal actuation scanning such as micromotors [16, 17]. Micromotor catheters were first demonstrated in 2004 and enabled precise beam scanning at a slow frame rates of 1-2 frames per second (fps) which are difficult to achieve by proximal scanning [16, 17]. These studies were limited by the speed of early time domain OCT systems (<2 kHz A-scan rate). Later studies with swept source OCT demonstrated volumetric endoscopic imaging using micromotor catheters small enough to pass through the accessory port of the endoscope [18, 19]. Recently, our group demonstrated ultrahigh speed endoscopic OCT using a MEMS-tunable vertical-cavity surface-emitting laser (VCSEL) light source and a micromotor imaging catheter in the rabbit [20] and human GI tracts *in vivo* [21]. The VCSEL light source enables ultrahigh speeds with MHz A-scan rates [20, 22] while the micromotor enables imaging at a high frame rate with minimal NURD [19, 23], which can be further corrected using fiducial based, non-rigid registration algorithms [24].

OCT angiography (OCTA) has been used to visualize three-dimensional (3D) microvasculature using the Doppler effect to isolate blood flow from the static tissue [25, 26]. OCTA was later performed using motion contrast, by calculating the amplitude, phase, or complex amplitude variation of the OCT signals between neighboring B-scan frames [27]. Amplitude-based OCTA relaxes system phase stability requirements and has good sensitivity to slow blood flows in the capillaries [28–32]. In addition, the majority of microvasculature is oriented transverse to the OCT beam, and thus it is difficult to visualize with Doppler OCT

because of the small axial phase shift from the Doppler effect. However, performing OCTA endoscopically has been challenging. Early studies suggested the feasibility of identifying 2D blood flow in the human GI tract and 3D blood flow in the living swine, but did not visualize microvasculature [5, 33]. Utilizing the ultrahigh imaging speed provided by VCSEL light sources and precision distal rotary scanning micromotor catheters, our group demonstrated OCTA imaging of 3D microvasculature in the human GI tract [21]. However, the imaging field of the micromotor catheter was limited by its small circumference, which made it difficult to survey large regions of the esophagus. Therefore, it is desirable to have an imaging technology for wide field, circumferential OCT and OCTA imaging of the esophagus.

In this study, we have developed a micromotor balloon imaging catheter to provide circumferential structural and angiographic imaging of the esophagus using an ultrahigh speed endoscopic OCT system. The OCT system has a 1.2 MHz A-scan rate and a $\sim 8.5 \mu\text{m}$ axial resolution in tissue using a 1310 nm wavelength MEMS tunable VCSEL light source. The micromotor balloon catheter provides volumetric OCT imaging of the esophagus over a 5 cm \times 2.6 cm (circumference \times longitudinal) area in <18 seconds. The micromotor enables precision rotary beam scanning at a frame rate of 240 fps. An improved NURD correction algorithm suppresses artifacts from the non-uniform micromotor scanning and physiological motion. The study demonstrates co-registered OCT and OCTA images of the swine esophagus *in vivo* as an important translational step toward human studies.

2. Material and methods

2.1 Swept source OCT imaging system

Figure 1 shows a schematic of the ultrahigh speed endoscopic OCT system used in this study, similar to the system recently reported [20, 34]. A high speed, wavelength swept light source based on a 1310 nm MEMS tunable vertical-cavity surface-emitting laser (VCSEL) was driven at 600 kHz to provide 1.2 MHz A-scan rate (bidirectional sweep) [20, 22]. A semiconductor optical amplifier was used to generate an average power of $\sim 80 \text{ mW}$. Ten percent of light was coupled into a Mach-Zehnder interferometer (MZI). The MZI output connected to a dual balanced clock generator (Thorlabs, Inc., NJ) to externally clock a 4 GSPS, 12 bit, A/D acquisition card (ATS 9370, AlazarTech, Quebec, Canada). The laser sweep range was $\sim 115 \text{ nm}$, enabling OCT imaging with an axial resolution of $\sim 12 \mu\text{m}$ in air ($\sim 8.5 \mu\text{m}$ in tissue) without spectral shaping and a Nyquist imaging range of $\sim 1.6 \text{ mm}$ in air ($\sim 1.2 \text{ mm}$ in tissue) determined by the maximum MZI clock frequency of 1.1 GHz. The OCT interferometer was a dual circulator based Michelson interferometer (AC Photonics, CA).

The sample arm of the OCT interferometer included a custom 3D-printed patient interface unit (PIU) to connect to the micromotor balloon catheter. The proximal end of the catheter was connected to a motorized stage (Parker, CA) located inside the PIU. A helical scan pattern was generated by pulling back the torque cable inside the balloon sheath. The incident power on the tissue surface from the balloon imaging catheter was 38 mW, within the ANSI standard for skin exposure. The OCT system sensitivity was measured to be $\sim 102 \text{ dB}$ using an isolated reflection from a flat cleaved fiber with calibrated attenuation. A custom developed acquisition software in C++ was used to integrate data acquisition, beam scanning control (driving the micromotor and synchronizing with the translation stage), real-time image processing/display and data storage.

2.2. Micromotor balloon imaging catheter

Figure 2(a) shows the schematic diagram of the micromotor imaging catheter, similar to previously published designs [20] but modified to extend the working distance for a balloon. The distal optics of the imaging catheter were comprised of two separated parts: a 2 mm outer diameter (OD) brushless DC micromotor (Namiki Precision, CA), and an optical focuser consisting of a 1 mm OD fiber pigtail/ferrule and a plano-convex lens (1.5 mm OD, 2 mm focal length, Edmund Optics, NJ) with an 11 mm working distance. Due to their small size, precise alignment, centering and mounting were required for both components. A custom

machined brass housing (Kroll Technologies, PA) housed and encapsulated the distal end components, which featured a three-strut design [35] with a $\sim 20^\circ$ circumferential extent for each strut to provide sufficient mechanical strength while achieving large ($\sim 300^\circ$) field of view (FOV). Individual struts were separated by 120° along the circumference. A 45° , 1 mm microprism (Tower Optical, FL) was slightly tilted and mounted on the micromotor shaft to deflect the optical beam by $<90^\circ$ towards the tissue while avoiding specular reflection. The focused spot size was $\sim 30 \mu\text{m}$ (full width at half maximum, FWHM in air). A 2 m long torque cable (2.2 mm OD, Asahi Intecc, CA) was used to connect the distal optics assembly. The rigid length and OD of the micromotor catheter was ~ 16 mm and 2.6 mm, respectively.

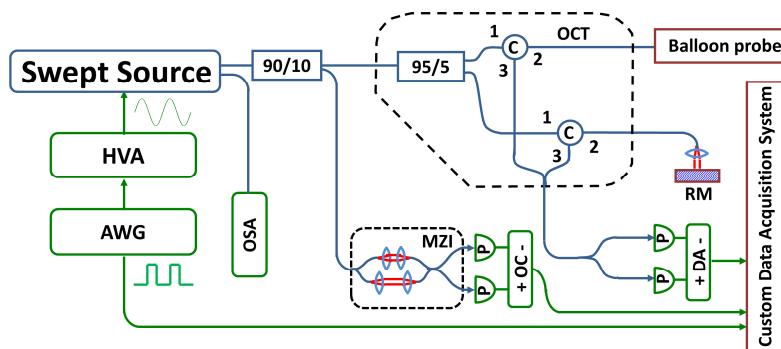


Fig. 1. Schematic of the ultrahigh speed endoscopic OCT system. HVA: high voltage amplifier; AWG: arbitrary waveform generator; OSA: optical spectrum analyzer; MZI: Mach-Zehnder interferometer; C: circulator; P: photodetector; OC: optical clock, DA: differential amplifier; RM: reference mirror.

The balloon sheath included a 16 mm OD (~ 5 cm circumference), 40 mm length, $\sim 55 \mu\text{m}$ thick polyethylene terephthalate (PET) balloon (Vention Medical, NH) at the distal end of a plastic sheath as shown in Fig. 2(b). The proximal neck of the balloon was removed to fit the OD of the plastic sheath (Zeus Industrial Products, SC), consisting of two polytetrafluoroethylene (PTFE) tubings. The inner PTFE sheath (AWG 9, 3 mm ID, 3.4 mm OD) allowed the micromotor imaging housing to translate within the sheath and perform a helical scan pattern with minimal friction. The space between the inner and outer PTFE sheath (AWG 7, 3.8 mm ID, 4.2 mm OD) was used to inflate/deflate the distal balloon. This design combines reusable micromotor imaging catheters and disposable balloon sheaths, and thus provides a cost-effective solution. In this study, the micromotor rotation speed was set to 14,400 RPM (240 fps) to ensure a sampling interval of $\sim 10 \mu\text{m}$ per A-scan, ~ 1.5 times Nyquist sampling along the circumferential direction. The pullback speed of the micromotor imaging catheter was 1.5 mm/sec, resulting in a $6 \mu\text{m}$ sampling interval between frames (~ 2.5 times Nyquist). High density sampling along the pullback direction was essential to perform endoscopic OCTA, which will be described in detail in section 2.4. The total acquisition time for each 3D-OCT data set (5000 x 4200 A-scans) was <18 seconds, which corresponds to a volume size of 50 mm x 26 mm x 1.2 mm (rotary x pullback x axial direction) in tissue. Figure 2(c) shows a photograph of the distal end of the micromotor balloon imaging catheter.

2.3 Nonuniform rotation distortion (NURD) correction

The micromotor imaging catheter does not require proximal rotation via the torque cable, and can be actuated at higher rotational speeds. The micromotor catheter exhibits significantly improved NURD performance compared with proximal rotary scanning [24, 36, 37]. Using a fiducial based correction algorithm, residual NURD in the OCT images can be corrected [24]. However, in the current study, the increased radius of the micromotor balloon catheter compared with a small micromotor catheter exacerbated the effect of rotary scanning instability. In addition, physiological motion (e.g. respiration or cardiac beating) near the GI

tract introduced artifacts when using a balloon catheter [36]. Therefore, fiducial based correction registration was insufficient.

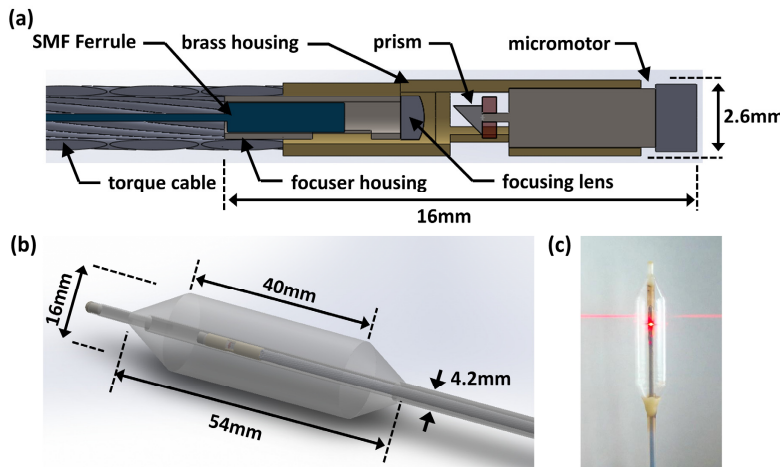


Fig. 2. Micromotor balloon imaging catheter. (a, b) Schematics of the micromotor imaging catheter and the balloon sheath respectively. (c) Photograph of the distal end of the micromotor balloon imaging catheter.

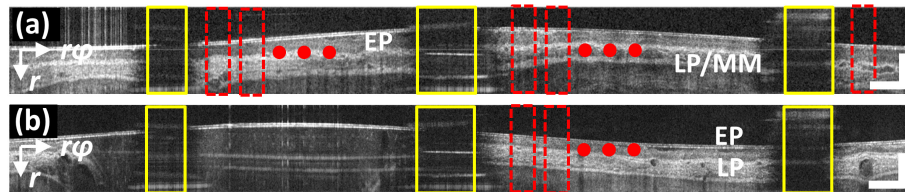


Fig. 3. Correction of nonuniform rotational distortion (NURD) from the micromotor scanning and physiological motion. (a, b) Cross-sectional OCT image of the swine esophagus, where the esophagus was not fully in contact with the balloon catheter during imaging in (b). Multiple regions of interest (ROIs) were selected from locations of the metal struts (yellow box) and tissue structures in multiple zones (red boxes and red dots) to remove the motion artifacts in the images. Scale bars: 0.5 mm (axial) and 2 mm (lateral). EP: epithelium; LP: lamina propria. r ϕ : circumferential direction; r: radial (axial) direction.

Figure 3 shows cross-sectional OCT images of the swine esophagus using the micromotor balloon catheter displayed in polar (unwrapped) coordinates. The FOV was split into three zones ($\sim 100^\circ$ FOV each) by brass housing struts (yellow box). The rotary (circumferential) direction is labeled as $r\phi$, indicating the scaling of this direction, and the radial (axial) direction is labeled as r in the cross-sectional OCT images. The characteristic layered architecture of squamous mucosa is seen (Figs. 3(a) and 3(b)). Our previous method used the metal strut edges in the cross-sectional OCT images as fiducial markers to measure the instantaneous rotational speed of the micromotor [24]. These locations were used to cubic spline resample the OCT data, such that the pixels in the transverse direction were spatially equally spaced. In this study, we extended this algorithm to measure the instantaneous rotational speed using multiple ROIs within the frames. The ROIs were selected at the three metal strut locations (e.g. yellow boxes, Fig. 3), as well as the tissue structures in individual zones (e.g. red boxes, Fig. 3) in the cross-sectional OCT images. In general, at least two ROIs were selected from the locations of individual metal struts, which accounts for >6 ROIs per cross-sectional OCT image. However, the number of ROIs corresponding to the tissue structures might vary between different 3D-OCT data sets, depending on the tissue contact with the balloon catheter and OCT signal quality. For example, as shown in Fig. 3(a), the tissue contact was good in all three zones. Thus, ~ 14 ROIs were selected from the three zones

in total. Conversely, the tissue contact was limited in one of the zones in Fig. 3(b). Therefore, only ~10 ROIs were selected from two zones with tissue contact in Fig. 3(b). Selection of the ROIs was done manually in this study by loading a representative frame and selecting regions with good tissue contact and low specular reflections. For regions where the tissue contact varied rapidly, the measurement of instantaneous rotation speed might be confounded by tissue motion such as the esophageal tissue sliding over the balloon surface. Specular reflections were sensitive to alignment of the OCT beam and balloon surface and were not reliable enough as a fiducial marker to estimate NURD. However, this process can be automated by employing segmentation algorithms.

After selection of ROIs, the instantaneous rotational speed at each ROI is measured by calculating the cross-correlation of individual ROIs between sequential cross-sectional frames. The algorithm calculates the transverse shift-translation between individual ROIs on a sub-pixel level [38]. Rotational speeds for all transverse pixels were then estimated by applying a cubic spline interpolation to the rotational speeds of the ROIs. Finally, a cubic spline resampling was applied to the OCT data to produce equal spacing between the transverse pixels. This method allows estimation of rotational velocity at multiple locations within the frames (not only strut locations), improving motion correction accuracy. Furthermore, using ROIs on the tissue as the fiducial markers also corrects for artifacts caused by physiological motion [36]. However, the disadvantage is that sequential frames need to be highly oversampled to enable calculation of the cross-correlations. Furthermore this method will not correct for motion which is perpendicular to the image plane. The NURD-correction algorithm described here is a subset of more general non-rigid image registration algorithms. Many of these algorithms estimate a displacement field (circumferential displacements for all A-scans in an image) by maximizing similarity between images while penalizing motion. We expect that a fully automated algorithm with improved performance should be possible using more advanced, non-rigid registration methods [39].

2.4 Endoscopic OCT angiography and data visualization

Prior to calculating the intensity decorrelation between consecutive cross-sectional OCT images, the non-rigid registration algorithm (section 2.3) was applied to generate NURD-corrected 3D-OCT data sets. Then, intensity decorrelation between sequential registered cross-sectional OCT images in linear OCT signal was calculated to generate cross-sectional OCTA images (decorrelation images) using the equation, where A_n is the OCT signal amplitude.

$$D_n(x, z) = 1 - \frac{A_n(x, z)A_{n+1}(x, z)}{\frac{1}{2} [A_n^2(x, z) + A_{n+1}^2(x, z)]}. \quad (1)$$

Following the decorrelation calculation, a moving average of three consecutive decorrelation images was taken to suppress the background decorrelation noise. Finally, a threshold mask was applied to the averaged cross-sectional OCTA images to remove regions with low OCT signal where the OCTA data is invalid [21, 24, 32]. In this study, an empirical threshold of ~mean (background noise) + 1.6 x standard deviation (background noise) was used.

The balloon surface in the NURD-corrected 3D-OCT data set was automatically detected using a graph cut based segmentation algorithm [40]. Each cross-sectional OCT and OCTA image were aligned radially with respect to the identified balloon surface to generate surface aligned/flattened NURD-corrected 3D-OCT and 3D-OCTA data sets. *En face* OCT and OCTA images were generated from the surface aligned/flattened NURD-corrected 3D-OCT and 3D-OCTA data sets using mean projection over a depth range of 50 μm at various depth levels beneath tissue surface. *En face* OCT images were displayed using square root compressed grayscale, while the cross-sectional OCT images were displayed using logarithmic grayscale. *En face* OCTA images were displayed using a linear gray scale.

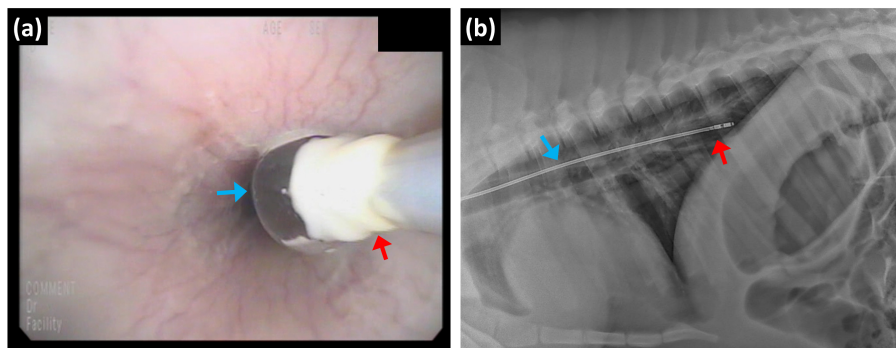


Fig. 4. (a) White light endoscopy image showing the positioning of the micromotor balloon imaging catheter in the swine esophagus. Blue arrow: inflated balloon; red arrow: joint between proximal end of the balloon and plastic sheath. (b) X-ray showing the position of micromotor balloon catheter in the swine esophagus. Blue arrow: torque coil of the micromotor catheter; red arrow: distal optics assembly.

2.5 Animal imaging procedures

OCT imaging was performed under a protocol approved by the Committee of Animal Care (CAC) at the Massachusetts Institute of Technology. Two female Yorkshire swine weighing approximately 30 kg were imaged in a single session. The anesthesia and sedation protocols are similar to previously reported [34]. Prior to the OCT imaging session, sedation was administered to each swine with intramuscular injection of 5 mg/kg telazol and 2 mg/kg xylazine, and atropine at 0.04 mg/kg was given to maintain heart rate and minimize mucus secretion. Before introducing the micromotor balloon catheter, a 16.7 mm ID overtube (Guardus, US Endoscopy, OH) was placed using a dual channel, upper GI endoscope (EG-3830, Pentax Medical). Once the overtube was in place, the endoscope was withdrawn and the micromotor balloon catheter was introduced through the overtube. The distal balloon was partially inflated (~10 psi) after the balloon catheter was positioned in the esophagus. Real time OCT imaging was used to confirm location in the upper GI tract. The endoscope was sometimes re-introduced to facilitate positioning the balloon catheter (Fig. 4(a)). X-ray images (Hudson Digital Systems, NJ) were also acquired to confirm positioning (red arrow, Fig. 4(b)). Once the catheter was positioned, the balloon was further inflated and maintained at a pressure of ~15 psi to improve the centering of the micromotor and optics in the lumen. After OCT imaging, the balloon was deflated prior to withdrawing the catheter from the esophagus.

3. Results

3.1 Demonstration of the NURD correction

Figure 5 shows results from the NURD correction algorithm for *en face* OCT and OCTA images of the swine esophagus. To highlight the improvements in contrast and quality, an enlarged region selected from the FOV ($\sim 13 \text{ cm}^2$) is shown. The standard deviation of the transverse shift of the individual ROIs between neighboring frames was $\sim 7 \text{ mrad}$ (median, $56.3 \mu\text{m}$ in circumferential position for the 16 mm OD balloon). Figures 5(a, d), (b, e) and (c, f) show *en face* OCT and OCTA images of the lamina propria (LP) before and after applying the NURD correction algorithm using ROIs from the metal struts alone, and both the metal struts and tissue structures, respectively. The improvement was less evident in the *en face* OCT images if only ROIs from the metal struts were used for NURD correction as shown in the magnified view (2X, insets, Figs. 5(a)-5(b)). *En face* OCT image contrast was improved more after further including ROIs from the tissue structures in the NURD correction (Figs. 5(a), 5(c)). In OCTA, NURD increases decorrelation noise (Fig. 5(d)). In addition, severe NURD between successive frames causes a spike in the OCTA decorrelation seen as a white

line motion artifact in the *en face* OCTA images (Fig. 5(d)). The decorrelation noise as well as the white line artifacts in the *en face* OCTA image were decreased significantly or removed using the NURD correction algorithm with ROIs from both the metal struts and tissue architecture (red arrows, Fig. 5(f)). In addition, the contrast of the smaller vessels in the *en face* OCTA image was improved, enabling visualization of microvasculature that was hard to identify prior to applying the correction algorithm. A rich and intricate vascular network mixed with larger-sized vessels was identified in the LP (Fig. 5(f)).

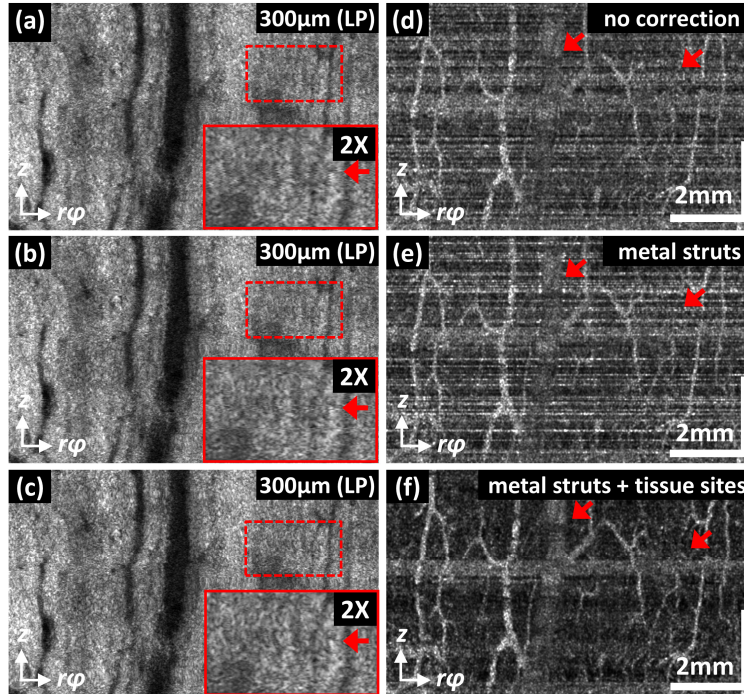


Fig. 5. Demonstration of the NURD correction algorithm for *en face* OCT and OCT angiography (OCTA) images. (a, d), (b, e), and (c, f) Co-registered *en face* OCT and OCTA images of the lamina propria (LP) layer of the swine esophagus from 300 μm beneath tissue surface before and after motion correction using regions of interest (ROIs) from the metal struts alone compared with both metal struts and tissue sites, respectively. Insets: magnified view (2X) from the selected region (dashed boxes, a-c) demonstrated that NURD between neighboring frames was significantly reduced (red arrows). In OCTA, decorrelation noise and white line motion artifacts were reduced, and image contrast was improved after NURD correction (red arrows, e-f). $r\varphi$: circumferential direction; z : longitudinal pull back direction. The same signal thresholds were applied for (a), (b) and (c), as well as for (d), (e) and (f).

3.2 Swine esophageal imaging

Figure 6 shows representative cross-sectional OCT images of the swine esophagus in both polar and Cartesian coordinates. The epithelium (EP), lamina propria (LP), muscularis mucosa (MM), and submucosa (SM) of the squamous mucosa were identified in the OCT images (Figs. 6(a), 6(b)). Regions not fully in contact with the balloon surface were observed in the 12 and 6 o'clock locations in Fig. 6(b) where the contact level varied because of cardiac motion ([Visualization 1](#)). The circumferential view (Cartesian coordinate) was displayed using a 4:1 aspect ratio. In the magnified view (3X) of the ROI in the cross-sectional OCT image (Fig. 6(a)), detailed layered architecture of normal swine esophagus can be appreciated more clearly, along with the presence of small vessels (star mark, Fig. 6(c)). Figure 6(d) shows a 3D rendering of the esophagus. The circumferential FOV was decreased from 360 to 300 degrees due to the metal struts in the imaging catheter (red arrows, Fig. 6(b)). Shadowing from a large vessel was also observed (blue arrow, Fig. 6(d)).

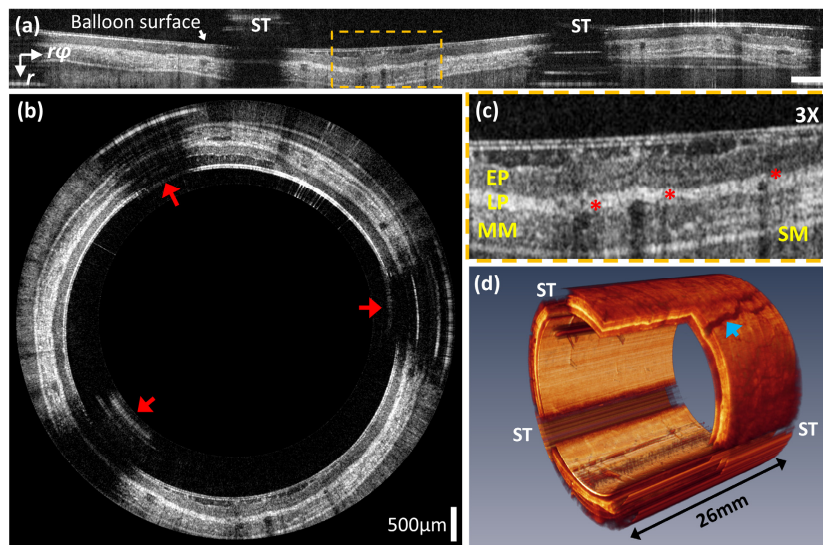


Fig. 6. Micromotor balloon OCT of the swine esophagus *in vivo*. (a, b) Representative cross-sectional images in polar and Cartesian coordinates. The Cartesian image is shown with a 4:1 aspect ratio. (c) Magnified view (3X) of the cross-sectional OCT image from the region of interest (dashed box, (a)) shows epithelium (EP), lamina propria (LP), muscularis mucosa (MM), and submucosa (SM) of normal esophagus. Small vessels in the LP (star) are also visible. (d) Rendering of the esophagus. Blue arrow: shadowing from a large vessel. ([Visualization 1](#)). ST: circumferential regions blocked by metal struts. Scale bars in (a): 0.5 mm (axial) and 2 mm (lateral). $r\varphi$: circumferential direction; r : radial (axial) direction.

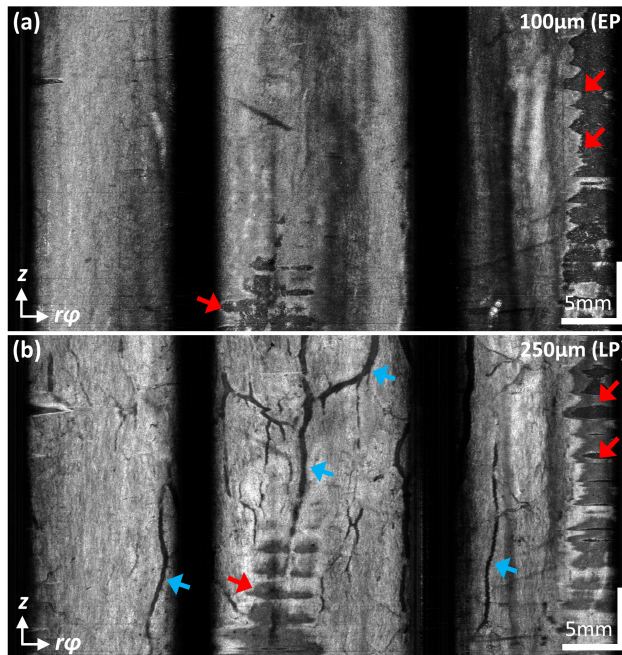


Fig. 7. (a, b) *En face* OCT of the swine esophagus from $\sim 100 \mu\text{m}$ (mean projection from 75 to $125 \mu\text{m}$) and $250 \mu\text{m}$ (mean projection from 225 to $275 \mu\text{m}$) below surface correspond to the epithelium (EP) and the lamina propria (LP) layer, respectively. Tissue contact varied along the pullback direction (red arrows) because of cardiac motion. Shadowing from the shallower vessels can be seen (blue arrows). ([Visualization 2](#)). $r\varphi$: circumferential direction; z : longitudinal direction.

En face OCT images of the normal swine esophagus were reconstructed from the 3D-OCT data set in Fig. 6 following processing steps described in section 2.4. Figure 7(a) shows the *en face* OCT image obtained using a mean projection from 75 to 125 μm below the tissue surface, corresponding to the EP layer, showing a homogeneous tissue composition. However, variation in tissue contact can be noted as an oscillating tissue boundary along the pullback/longitudinal direction (red arrows). The *en face* OCT images are displayed oriented with the top and bottom of individual images corresponding to longitudinal direction from the proximal to distal end of the esophagus. Figure 7(b) shows the *en face* OCT image obtained by mean projection from ~ 225 to 275 μm below the surface showing the LP where shadowing from a large vessel is seen (blue arrows) along with an oscillating tissue boundary (red arrows) due to cardiac motion.

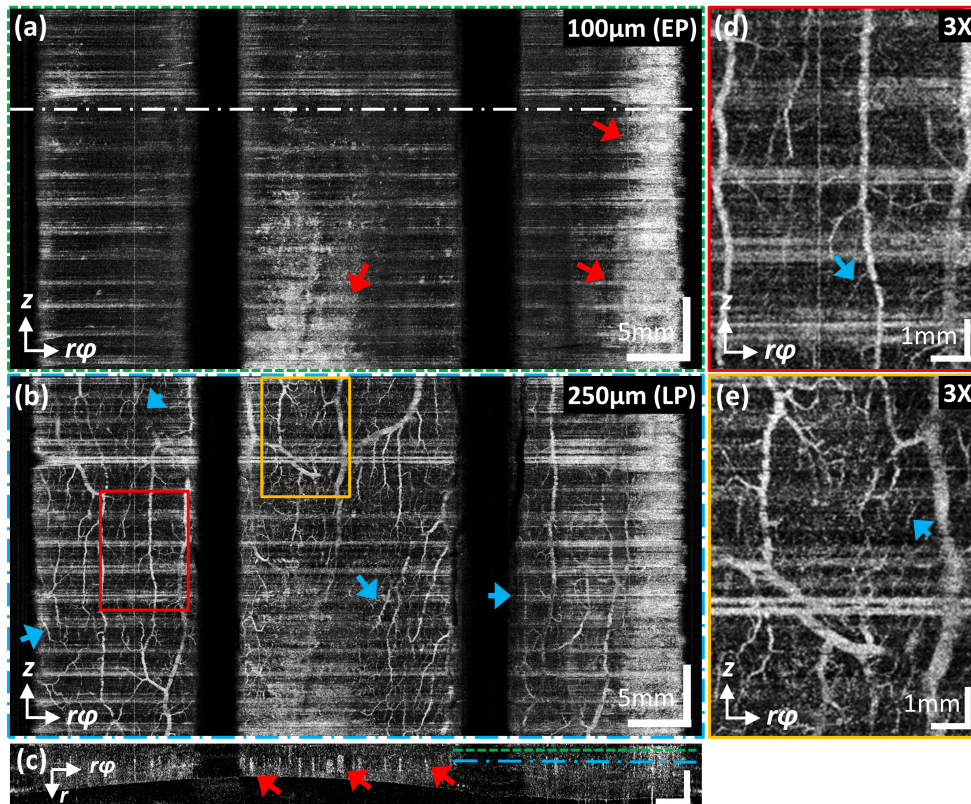


Fig. 8. (a, b) *En face* OCTA of the swine esophagus from 100 μm (mean projection 75 to 125 μm) and 250 μm (mean projection from 225 to 275 μm) below tissue surface, corresponding to the epithelium (EP) and lamina propria (LP) layer, respectively. Tissue contact varied along the pullback direction (red arrows) from cardiac motion, resulting in high decorrelation near the tissue boundary. Microvascular networks are seen in the LP layer (blue arrows). (Visualization 3). (c) Cross-sectional OCTA image from the location in (a) marked by white dashed-dotted line. The locations of the microvasculature can be identified from regions exhibiting high decorrelation signals (red arrows). The depth locations of the *en face* OCTA images of the EP and LP layer (a, b) are marked by green and blue lines, respectively. (d, e) Magnified (3X) view of the OCTA from region of interest marked (b) where the small vessels can be observed more clearly (blue arrows). $r\varphi$: circumferential direction; z : longitudinal pull back direction; r : radial (axial) direction. Scale bars in (c): 0.25 mm (axial) and 2 mm (lateral).

Figure 8 shows coregistered *en face* OCTA images at different depths. In Fig. 8(a), high decorrelation signal was observed where the tissue lost contact with the balloon. Debris in the space between the balloon and esophagus as well as tissue movement from cardiac motion generated high decorrelation (red arrows). Figure 8(b) shows *en face* OCTA images of the LP

layer from a 225 to 275 μm mean projection below the tissue surface. The microvascular pattern in Fig. 8(b) is finer than in Fig. 7(b), where vasculature is seen because of shadowing effects. An intricate microvascular network can be appreciated across most of the visible FOV. In the region on the right, the increased decorrelation noise on the background might be due to varying tissue contact from cardiac motion. About 14 oscillatory periods are seen in the decorrelation signal on the left in Fig. 8(a), consistent with the swine heart rate.

Figure 9 shows coregistered *en face* OCT and OCTA images of the distal esophagus including the gastroesophageal junction (GEJ) from $\sim 250 \mu\text{m}$ (mean projection from 225 to 275 μm) below the tissue surface. Tissue contact was limited in the gastric region because the esophagus opens into the stomach distal to the GEJ (Fig. 9(a)). In the region having reasonable tissue contact on the gastric side, contact was unstable and varied along the pullback direction (red arrows), possibly because of cardiac motion. At the GEJ, the effect of cardiac motion can be more pronounced than in regions away from GEJ, such as the middle esophagus. This motion made it challenging to identify gastric microvasculature because of insufficient tissue contact and increased decorrelation noise. However, if the tissue contact was sufficient, such as in the squamous epithelium near the GEJ, fine microvasculature can be observed from 250 μm (mean projection from 225 to 275 μm) beneath tissue surface (Fig. 9(b)) albeit with higher decorrelation noise compared to Fig. 8.

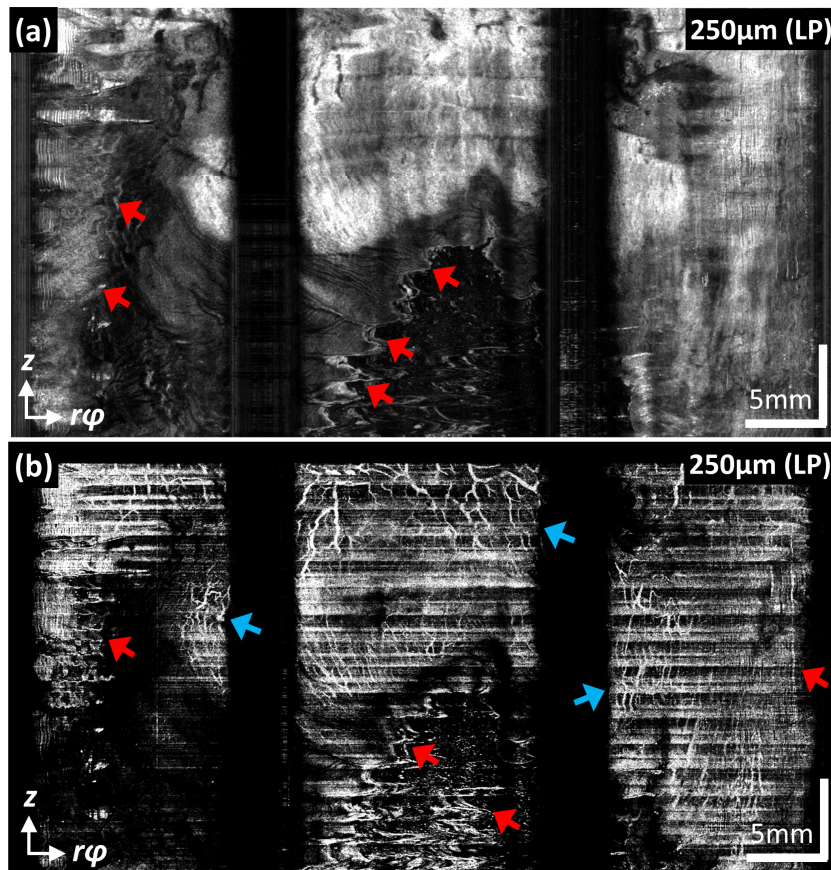


Fig. 9. (a, b) Coregistered *en face* OCT and OCTA images of the swine distal esophagus including the gastroesophageal junction (GEJ) from about 250 μm (mean projection from 225 to 275 μm) beneath tissue surface, corresponding to the lamina propria (LP) layer in the squamous mucosa. As a result of the opening after GEJ, the tissue contact was poor in the gastric mucosa (red arrows, (a, b)). Fine microvasculature in the LP layer can be observed in the squamous mucosa (blue arrows, (b)) ([Visualization 4](#)). $r\varphi$: circumferential direction; z : longitudinal direction.

The cross-sectional OCTA image from the location highlighted in Fig. 8(a) showed regions of high decorrelation signals from blood flow in the microvascular network. In addition, speckle decorrelation tails (OCTA projection artifacts) below the vessels were observed (red arrows, Fig. 8(c)). Artifacts from the volumetric data flattening operation were also present. Magnified views from the ROIs in Fig. 8(b) better visualized the intricate microvascular network in the LP (Figs. 8(d), 8(e)). The size of the smallest vessels in the magnified views was ~40-50 μm diameter (blue arrows), close to the focused OCT beam size.

4. Discussion

Mucosal surface patterns have been widely investigated to detect regions of dysplasia in BE using several endoscopic imaging techniques including chromoendoscopy [14], narrow band imaging (NBI) [41], and confocal laser endomicroscopy (CLE) [42]. Although studies from expert imaging centers showed promising results with high dysplasia detection accuracy [43], data establishing widespread utility is still lacking. Chromoendoscopy requires topical application of stains, a cumbersome procedure which might obscure the endoscopic view after contrast agent application. CLE also requires administration of contrast agents, typically IV fluorescein [42]. In addition, the imaging field is limited to $<0.1\text{mm}^2$ with the probe based CLE system, making it vulnerable to motion and difficult to assess large areas for pathology.

En face OCT allows rapid assessment of mucosal surface patterns, similar to conventional WLE, but with depth resolution. Our group recently demonstrated high contrast *en face* OCT images of normal human esophagus and patients with BE and dysplasia, although the imaging coverage was limited to $\sim2\text{ cm}^2$ using small micromotor catheters [21]. Recently, we also showed *en face* OCT images over a longitudinal extent of the esophagus in living swine using a micromotor capsule [34]. However, contact with the full esophageal circumference is challenging with capsule devices, and studies by other groups reported $\geq50\%$ tissue contact in 94% of the OCT images [44]. This might make capsule imaging more vulnerable to sampling errors than balloon catheters. In addition, balloon catheters can potentially pass through the accessory port of the endoscope as shown in current commercially available balloon based OCT systems. This facilitates collection of co-registered biopsies or administration of endoscopic therapies in conjunction with OCT imaging.

Combining the merits of micromotor and balloon catheters, the technology shown in the current study can provide volumetric cross-sectional and *en face* OCT images of the esophagus. *En face* OCT images of the swine esophagus with $>90\%$ coverage of esophageal circumference over a $\sim2.6\text{ cm}$ longitudinal extent were demonstrated. Cross- sectional and *en face* OCTA images can be obtained over a wide field of view, but require oversampling and therefore reduce the area coverage compared to structural OCT alone. At the same time, *en face* OCTA images have distinctive features and data can be rapidly inspected and compared with structural OCT. This promises to facilitate the diagnostic reading of volumetric data.

Angiogenesis is known to have an essential role in the progression from nondysplastic BE to dysplasia [45]. It has been suggested that the ability to identify atypical microvasculature in BE might facilitate detection of dysplasia [46]. Several endoscopic imaging modalities such as NBI and CLE can increase vascular contrast. However, NBI only visualizes surface vascular patterns. Although CLE can provide subsurface imaging of microvasculature using exogenous contrast agents, it has a limited FOV and only superficial vasculature can be visualized. OCTA has the advantage that it can perform depth resolved imaging over large fields of view.

Studies investigated Doppler OCT to provide vascular information of the GI tract, measuring blood flow in the large vessels within or below the muscularis mucosa layer [5, 33]. Conversely, OCTA techniques can visualize smaller vessels with slow flow, which are difficult to see with Doppler OCT. The majority of microvasculature is oriented transverse to the OCT beam and thus is difficult to visualize using the Doppler effect, which is sensitive to axial flow. Our group recently demonstrated the feasibility of using endoscopic OCTA to visualize subsurface vasculature in patients with dysplastic BE using small micromotor catheters [21]. However, the imaging coverage of endoscopic OCTA in this study was

limited. Although the diagnostic performance of endoscopic OCTA for detecting dysplasia in BE is still under evaluation, the ability to acquire densely sampled and motion corrected volumetric OCT and OCTA data, enabling both *en face* and cross-sectional views is important for future clinical applications as well as fundamental studies.

Endoscopic OCTA requires a higher sampling density compared with structural OCT, because it uses motion contrast to visualize microvasculature. Assuming a focused spot size of $\sim 30\text{ }\mu\text{m}$, the longitudinal sampling interval for OCTA in the current study is $\sim 6\text{ }\mu\text{m}$, compared to the Nyquist sampling interval of $15\text{ }\mu\text{m}$. The dense sampling in OCTA increases the acquisition time to survey the esophagus. In addition, since OCTA detects motion, it is more vulnerable to physiological motion artifacts. The imaging speed can be improved by increasing the frame rate of the catheter as well as the A-scan rate of the light source. However, for a given laser exposure, detection sensitivity will decrease inversely proportionally to A-scan rate. In addition, the imaging range will decrease for fixed A/D sampling speeds. Decreased sensitivity can decrease the performance of OCTA especially the ability to detect small vessels or capillaries. An alternative approach would be to rapidly survey the esophagus with Nyquist sampling and then scan with dense sampling to acquire OCT microvasculature information over ROIs with suspicious structural abnormalities.

In addition, the imaging range of the current system was 1.2 mm in tissue due to the A/D sampling, limited by the optical clock module electronics. Although balloon catheters provide stable scanning, centration of the micromotor and optics can vary with flexure of the central sheath, causing changes in range. Flexure is more pronounced if the esophagus has a complex or tortuous geometry, such as in a stricture near the gastroesophageal junction (GEJ) or a hiatal hernia. The imaging range can be improved by increasing the optical clock electronic bandwidth to operate at the full A/D card rate. The VCSEL light source drive waveform can be modified to provide a linearized frequency sweep and improve imaging range. Alternatively, an acoustic-optical modulator [47] or a silicon photonic integrated IQ receiver [48] can be used to remove the complex conjugate ambiguity in the OCT imaging and double the imaging range. However, if variations in centration of the optics are larger than the focusing depth of field, the transverse image resolution will be degraded.

The size of the micromotor balloon catheter in this study was too large to fit in the 3.7 mm endoscope accessory port (GIF-2TH180, Olympus) even after deflating the balloon. Although the current balloon catheter can still be introduced via an overtube, it is desirable to further reduce the size to allow passage through the accessory port. A 2 mm OD micromotor and a $\sim 4.2\text{ mm}$ OD plastic sheath were used in this study. However, micromotors with ODs as small as 1 mm have been reported in recent studies [23]. A customized balloon with desired OD, length, distal and proximal neck can be fabricated. The OD of the plastic sheath used in this study increases the rigidity of the balloon catheter and can be decreased.

There are many approaches which can be used for motion/NURD correction as well as for signal processing in OCTA. The methods demonstrated in this study may not be optimal, but demonstrate the feasibility of the imaging platform. Improvements in motion correction, OCTA processing as well as mechanical design should improve performance in the future, enabling even smaller vessels to be visualized.

Future development of the micromotor balloon catheters promises to enable an integrated platform combining high speed OCT imaging with other endoscopic capabilities. Studies have demonstrated laser marking of biopsy sites for OCT-guided biopsy procedures with distally scanned balloon catheters [49]. Laser thermal coagulation has also been suggested as a therapy for dysplastic BE [50]. Micromotor balloon catheters can improve the beam scanning and positioning accuracy compared with distal scanning, improving laser marking as well as laser beam scanning for treatment.

5. Conclusion

In this study, we demonstrated a micromotor balloon imaging catheter and an ultrahigh speed OCT system with a 1.2 MHz A-scan rate, imaging at 240 frames per second. The micromotor balloon catheter enabled comprehensive volumetric imaging of the swine esophagus. An

improved non-rigid registration algorithm corrected artifacts from the micromotor catheter and physiological motion. *In vivo* coregistered *en face* OCT and OCTA images of swine esophagus were demonstrated. OCTA can provide volumetric microvascular information which may be markers of dysplasia in Barrett's esophagus. This technology promises to facilitate imaging in existing balloon based endoscopic OCT systems, and demonstrates a translational milestone toward volumetric *en face* OCT and OCTA in patients.

Acknowledgments

This work was supported in part by the National Institutes of Health R01-EY011289-30, R44-EY022864-03, R01-CA075289-18, R44-CA101067-05, R01-CA178636-03, R37-EB000244-36, and Air Force Office of Scientific Research (AFOSR) contracts FA9550-10-1-0063 and FA9550-12-1-0499. The authors thank Dr. Jennifer Haupt and Morgan Jamiel of the M.I.T. Division of Comparative Medicine for veterinary support. The authors also thank Dr. Tsung-Han Tsai (St. Jude Medical) for helpful discussion on the balloon catheter. Kaicheng Liang acknowledges support from the Agency for Science, Technology and Research (Singapore).